

Citation for published version:

Chen, D, Li, W & Hall, P 2018, 'Motion Estimation and Segmentation of Natural Phenomena', Paper presented at 29th British Machine Vision Conference, BMVC 2018, Newcastle, UK United Kingdom, 3/09/18 - 6/09/18.

Publication date:
2018

Document Version
Peer reviewed version

[Link to publication](#)

University of Bath

Alternative formats

If you require this document in an alternative format, please contact:
openaccess@bath.ac.uk

General rights

Copyright and moral rights for the publications made accessible in the public portal are retained by the authors and/or other copyright owners and it is a condition of accessing publications that users recognise and abide by the legal requirements associated with these rights.

Take down policy

If you believe that this document breaches copyright please contact us providing details, and we will remove access to the work immediately and investigate your claim.

Motion Estimation and Segmentation of Natural Phenomena

Da Chen
da.chen@bath.edu

Wenbin Li
wenbin.li@imperial.ac.uk

Peter Hall
P.M.Hall@bath.ac.uk

Department of Computer Science
University of Bath
Bath, UK

Imperial College London
London, UK

CAMERA
University of Bath
Bath, UK

Abstract

Dense motion estimation for dynamic natural phenomena (water, smoke, fire, *etc.*) is a significant open problem. Current approaches tend to be either general, giving poor results, or specialise in one phenomenon and fail to generalise. Segmentation of phenomena is also an open problem. This paper describes an approach to estimate dense motion for dynamic phenomena that is simple, general, and which yields state of the art results. We use our dense motion field to segment phenomena to above state of the art levels. We demonstrate our contributions using lab-based video, video from a public dataset, and from the internet.

1 Introduction

Accurate, dense motion estimation is a long-standing problem in Computer Vision. Several decades of research have produced impressive results. Motion estimation over a wide variety of different types of object is now possible: rigid bodies, articulated bodies, soft bodies. Yet a simple but general motion estimator for natural phenomena (smoke, fire, *etc.*) currently remains unavailable. Similar remarks apply to segmentation where many problem have been solved but the segmentation of natural phenomena remains difficult.

Simple but general solutions to these problems would benefit many diverse application areas. For example Computer Graphics has applications in both post-production [16, 18, 26] and model acquisition [22]. In atmospheric research, there are applications for storm identification and forecast [20], forecast and tracking the evolution of convective systems [5] and rain cloud tracking [9]. Our motivation derives from model acquisition and editing in the creative sector. Our approach using “skeletons” included a desire to provide entities to support editing, but a discussion of editing would take us well beyond the focus of this paper: the computer vision problems of flow estimation and segmentation.

This contributions of this paper are as follows. **First** to describe a simple method using “skeletons” for sparse flow estimation with an upgrade to dense flow estimation, and in particular to show that it generalises to several phenomena. Skeletons are sparse topographical maps over the phenomena. Empirical testing using laboratory based data, a public dataset for natural phenomena, and video from the internet “in the wild”) show our method significantly improve state-of-the-art accuracy above a representative range of both well established and current methods. **Second**, we show how to use our dense flow solution, including skeletons, to segment natural phenomena, exceeding state-of-the-art solutions.

2 Related Work

Optical flow [19] describes dense motion. Significant effort has been expended on real-world challenges *e.g.* large pixel displacement [2], non-rigid deformation [13] and rapid optimization [8, 12, 29], *etc.*

Most optical flow estimation approaches are based on a variational model which combines a data term with a regularising term. The former encodes a brightness constancy assumption while the latter constraints how the motion field can vary over space. Fluid motion is non-rigid and violates the brightness constancy assumption; but careful choice of the regularising term boosts performance. Example approaches include Aurox *et al.* [3] who utilise a group-wise appearance prior to regularize the flow; also Corpetti *et al.* [11] who impose divergence and curl smoothness to constraint fluid motion. Stronger physical models appeal to the Navier-Stokes (NS) equations to design a regulariser. Doshi *et al.* [13] replace the normal smoothness term with Navier-Stokes (NS) equation, which preserves general motion behaviour but often over-smooths details. To further smooth the motion, Anumolu *et al.* [4] propose vorticity confinement which blurs the internal boundaries. Li *et al.* [23] claim that NS equations can be applied together with 3D flow prediction in order to improve precision.

Others have used physical properties more directly. Sakaino [30] generates the properties of wave using sinusoidal functions to achieve dense fluid motion. Refractive properties are used in [20, 22]. These approaches give high performance in the laboratory environments but lead to errors on real-world cases.

Recent work has proven the importance of high-quality sparse flow estimations to initiate upgrades to dense flow. Revaud *et al.* [29] propose a novel sparse to dense interpolation to post-process the matching result of DeepMatch [39] and use it as an initial input for standard optical flow energy minimization process. Chen *et al.* [9] further improve the sparse match result and got state-of-the-art result using the same framework as EpicFlow [29]. Such work is of relevance here because we too begin with a sparse estimate, which is then upgraded to a dense estimate.

Segmentation of natural phenomena is difficult because they are diffuse, translucent, often have ill defined borders, and usually form part of a complex scene. There are some works in the literature on the subject. Xu *et al.* [40], and later, Ochs *et al.* [24] use multiple frames. Papazoglou and Ferrari [27] use optical flow to track superpixels over time to establish temporal coherence and further achieve the fast foreground segmentation. Teney *et al.* [34, 35] propose custom spatio-temporal filters, over a time window of about 7 or 8 frames, to separate spatial and temporal patterns – a learnable metric improves their segmentation on highly dynamic objects. Most recently, Cheng *et al.* [10] integrate segmentation and motion estimation by proposing an end-to-end trainable network; they provide good results in both segmentation and motion estimation. Due to the lack of ground-truth data, we cannot train this network on natural phenomena sequences, hence during experiments we applied the model provided by the authors to obtain test results.

Our flow estimator differs from all of the above. Its aims to be less specific than approaches premised on fluids, so we cannot appeal to Navier-Stokes or similar physical equations. As explained next, we use a two-stage approach, the first of which completely abandons the brightness constancy assumption to produce a sparse but global flow. This global flow then provides a starting point for a dense estimation that does use brightness constancy. Our algorithm for segmentation is also unique: it re-purposes the “skeletons” from the flow estimate, and requires only a pair of frames to exceed state of the art results.

3 Flow Estimation

As observed in Section 2, current motion estimation methods for natural phenomena either make weak but (in this case) invalid assumptions such as brightness constancy, or else make strong assumptions regarding the behaviour of fluids. We adopt neither of these to estimate a global flow. Instead, our method assumes that *the global shape of the phenomena under observation changes little between frames*. Specifically, we assume topographical maps, here called *skeletons*, in adjacent frames are

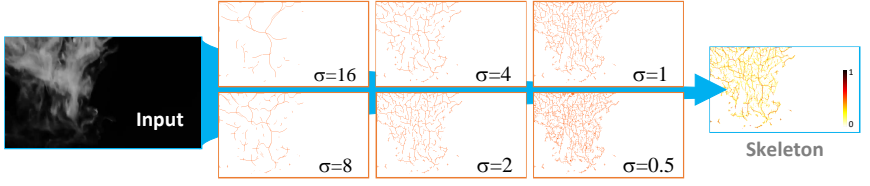


Figure 1: Given an input frame, a weighted skeleton is aggregated from binary skeletons generated different filtering scales. Although we use the as example to explain skeleton generation, the same applies to other natural phenomena.

similar. Our skeletons are maps of local intensity maxima, because this typically corresponds the the densest region of smoke / steam / fire *etc.* These skeletons do not change much between frames even if brightness changes it is likley to remain locally maximally, and being sparse makes skeletons easy to use to construct a sparse flow.

Our approach has three main steps: (1) construct a skeleton for each of two frames; (2) estimate a sparse flow; (3) upgrade sparse flow to dense flow (at which point we do allow brightness constancy to influence the solution). For segmentation, we segment with the aid of the skeleton. As results show, we obtain excellent results over a range of phenomena and videos from different sources.

3.1 Skeleton Construction

Constructing a skeleton is straightforward. Given a gray scale image, we blur it with a Gaussian kernel of scale σ , to obtain $f(\cdot)$. Next, we mark local horizontal maxima. There is horizontal maxima at pixel (x, y) if $f(x-1, y) \leq f(x, y) \leq f(x+1, y)$. Similarly, mark local vertical maxima over pixel columns. Finally, we combine these maps of maxima to make a binary skeleton by combining them with an ‘or’ operator. We construct a weighted *multi-scale skeleton* by the aggregation of binary skeletons at different scales:

$$h(\mathbf{x}) = \frac{1}{N} \sum_{j=1}^N h_j(\mathbf{x}), \quad (1)$$

with h_j being a binary skeleton image under blurring kernel σ_j , and \mathbf{x} is a point in the image. The result of this is a multi-scale skeleton that tends to emphasise stable structures within the phenomenon: higher values of the mutli-scale skeleton indicate locations that are more stable over scale. Figure 1 illustrates the skeleton building process.

3.2 Sparse Flow Estimation

We begin flow estimation by assuming that the motion of observed phenomena is subject to a very general transfer of mass $\rho_{t+dt}(\mathbf{y}) = \int_{\mathbf{x} \in \mathbb{R}^3} \phi(\mathbf{y}, \mathbf{x}) \rho_t(\mathbf{x}) d\mathbf{x}$ in which $\rho(\cdot)$ is local density, $\rho_t(\mathbf{x}) d\mathbf{x}$ is local mass, and ϕ is a mass transfer function that includes systematic motion, diffusion, *etc.* This is at best very hard to solve. Instead, we further assume points \mathbf{x} and \mathbf{y} lie in the plane \mathbb{R}^2 , that local density is proportional to observed pixel brightness, and we consider only points on one multi-scale skeleton. Specifically, we estimate the expected location of each point \mathbf{x} on a topographic skeleton $S_1 \subset \mathbb{R}^2$ when attracted by all points \mathbf{y} on a topographic skeleton $S_2 \subset \mathbb{R}^2$:

$$\mathbb{E}[\mathbf{y}|\mathbf{x}] = \sum_{\mathbf{y} \in S_2} \mathbf{y} p(\mathbf{y}|\mathbf{x}). \quad (2)$$

The expected point $E[\mathbf{y}|\mathbf{x}]$ is not constrained to lie on skeleton S_2 , but it is global in the sense that it takes all S_2 points into account. It does not rely on brightness, nor does it require any optimisation, so is very fast to compute.

The definition of $p(\mathbf{y}|\mathbf{x})$ is important. It is defined using spatial distance and intensity of the skeletal pixels, similar to a bilateral filter [86]

$$p(\mathbf{y}|\mathbf{x}) \propto \mathcal{N}(\mathbf{x}|\mathbf{y}, C_y) \mathcal{N}(h(\mathbf{x})|h(\mathbf{y}), \sigma_v). \quad (3)$$

in which $h(\cdot)$ is the value at a point in a multi-valued skeletal image (Eqn. 1). The term using them encourages a match between skeletal parts of about equal stability; the variance σ_v matters little; we set $\sigma_v = 1$. The spatial part of the attraction depends on a covariance C . For this we use a non-isotropic Gaussian that is aligned so that its longest principle axis is normal to the skeleton S_2 at \mathbf{y} . The covariance matrix $C_y = ULU^T$ is specified by:

$$U = [\hat{\mathbf{n}}, \hat{\mathbf{t}}], \quad (4)$$

$$L = \sigma \text{diag}([s, 1]). \quad (5)$$

The value of σ determines the effective range of the attraction, we set $\sigma = 1$, but a wide range of values suffice. The scale s determines the weight of the axis normal to the skeleton relative to the tangential axis. An isotropic Gaussian tends to attract points more strongly to the centre of skeletal lines, a tendency we wish to avoid. Therefore, we adopt an elliptical covariance with long-axis normal to the local skeleton mitigates against a build-up of probability density towards the centre of skeletal lines. A wide range of s value works well, in our experiments we set $s = 10$.

3.2.1 Improving the sparse estimate

We improve on the sparse estimate by also considering the ‘backward’ process (similar to [25]). That is, we also consider $E[\mathbf{x}|\mathbf{y}]$. In particular, we assume that the underlying physics governing the phenomenon are symmetric in time. Therefore, we estimate both sparse motion both forward and backward in time, and maintain only consistent results. In a little more detail, we consider sets with ‘forward elements’ ($\mathbf{x} \in S_1, E[\mathbf{y}|\mathbf{x}]$) and ‘backward elements’ ($\mathbf{x}' \in S_2, E[\mathbf{y}'|\mathbf{x}']$). To check the consistency, we use

$$\|x - E[\mathbf{y}'|\mathbf{x}']\|^2 + \|E[\mathbf{y}|\mathbf{x}] - \mathbf{x}'\|^2 < \delta. \quad (6)$$

This is equivalent to use KNN clustering to locate consistent forward and backward pairs. This process solves problems such as the appearance and/or disappearance of topographical features.

3.3 Dense Flow Estimation

We now upgrade a sparse flow to a dense flow. At this stage, we do use brightness constancy, along with other terms. The reason is that the sparse estimation is a global estimate which provides a sufficient prior constraint on the dense solution to make such assumptions reasonable. We want to estimate a vector field $\mathbf{v}(\mathbf{x})$ for all points \mathbf{x} in some segment of frame one, given a sparse estimate $\mathbf{v}(\mathbf{x}) = \mathbb{E}(\mathbf{y}|\mathbf{x}) - \mathbf{x}$. We use a two-step approach that is explained briefly here.

We first interpolate our sparse flow into a dense flow using a method proposed by Garcia *et al* [48], which is designed for natural phenomena. Setting $\mathbf{u} = [u_1, u_2]^T$ and $\mathbf{v} = [v_1, v_2]^T$ the interpolation process yields a new field v_k from sparse field u_k by the following energy minimization problem:

$$\underset{v_k}{\text{argmin}} \|v_k - u_k\|^2 + \lambda \|\nabla^2 v_k\|^2 \quad (7)$$

in which λ is a regularisation parameter that controls smoothness. We used a value for λ directly from the original paper.

Step two ‘polishes’ the new dense motion estimation by smoothing it using variational optical flow energy [8] and a smoothness term [41], which requires us to solve:

$$\begin{aligned} H(\mathbf{v}) = & \int_{\Omega} \underbrace{\phi(\|f_1(\mathbf{x} + \mathbf{v}) - f_2(\mathbf{x})\|^2)}_{\text{Brightness Constancy}} \\ & + \alpha \underbrace{\phi(\|\nabla f_1(\mathbf{x} + \mathbf{v}) - \nabla f_2(\mathbf{x})\|^2)}_{\text{Gradient Constancy}} d\mathbf{x} \\ & + \gamma \underbrace{\int_{\Omega} \phi(\|\nabla v_1\|^2 + \|\nabla v_2\|^2) d\mathbf{x}}_{\text{Smoothness Constraint}} \end{aligned} \quad (8)$$



Figure 2: Steps in frame segmentation, each step uses agglomerative clustering to merge super-pixels into image segments; colour, motion and skeletal density are used respectively.

where f_* denotes the input images and \mathbf{v} represents the smoothed flow field in between; $\nabla = (\partial_{xx}, \partial_{yy})^T$ is a spatial gradient and $\phi(s) = \varepsilon^2 \log(1 + s^2/\varepsilon^2)$ with $\varepsilon = 2$ penalizes the flow gradient norm. The energy function was defined as a combination of a data term (brightness constancy and gradient constancy). We used parameter values for α and γ quoted in the original paper. See our supplementary material for a more in-depth explanation of our dense upgrade.

4 Segmentation

Our algorithm for segmentation is outlined in Figure 2. The general idea is to merge superpixels [10] using a sequence of criteria, as explained next, there are three steps to the algorithm.

First, superpixels are merged into segments using spatial distance, which uses the Euclidean distance in the image plane, and colour similarity, which uses the mean colour in each superpixel. We specify it to be the Euclidean distance in CIE L*a*b* colour space. Superpixels are thereby clustered into larger superpixels.

Second, dense motion similarity is used next. We use only the direction of flow because we want to encourage grouping of super-pixels that move in a globally similar direction, regardless of speed. Therefore, we group on the basis of $\min(d\theta, 2\pi - d\theta)$ with the angle between flow vectors, *e.g.* $d\theta = \tan^{-1}u_2 - \tan^{-1}u_1$. The result is mid-sized areas, larger than super-pixels but smaller than region segments.

Finally we make use of the skeletal density. Skeletal density tends to be much lower than in the general background. This is especially marked in diffuse phenomena of interest here exhibit little surface texture, which can make them difficult for matching algorithms (and optical flow). We take advantage of this characteristic by defining skeletal density as the number of skeletal pixels per unit area, and continue to cluster on the basis of skeletal density similarity.

Despite the simplicity of this approach, experiments show it produces excellent results.

5 Empirical Evaluation

This section provides quantitative and qualitative evidence that our motion estimation and segmentation exceed state of the art for natural phenomena. Further evidence can be found in the supplementary material. Here we use videos of fire, steam, smoke, avalanches, landslides, boiling water, waterfalls, and volcanic eruptions. We used three classes of videos representing a progression from controlled conditions to “in the wild”: (i) High resolution video captured in our laboratory at a frame rate of 100 fps. (ii) Lower resolution video from established databases: Moving Vistas [63], Dyntex [17] and YUPENN DynSce dataset [12]. (iii) Video taken directly from the internet, of varying spatial resolution and a low frame rate typically. The “internet” videos include background motion clutter, and a computer graphic simulation. All experiments were run on consumer level laptops, using code written in a mixture of MATLAB and C++.

5.1 Dense Flow

We compare our approach to eight alternatives, using two different measures. We follow Li *et al.* [23] in comparing our method with general optical flow methods. FullFlow [60] and EpicFlow [29] are recent state-of-the-art algorithms that share a framework similar to our method. Classic+NL [63] provides robustness to motion discontinuity. HS [19] and BA [8] are classical optical flow methods

		Ours	FullFlow	EpicFlow	Class+NL	HS	BA	LDOF	MDP	FlowNet
Our Database	Thick_rise	61.60	128.12	166.78	100.03	93.48	100.15	160.14	136.48	135.9
	Thin_from_bottom	37.89	43.39	43.37	42.44	42.91	42.98	44.08	45.43	39.59
	Thin_drops_multi	58.25	73.32	68.12	65.76	67.16	68.33	64.59	68.14	67.03
	Orange_white_meet	37.89	46.56	41.21	42.14	44.94	43.66	41.75	42.79	42.64
	Slanted_surface_pour	41.00	59.63	57.73	57.18	56.8	59.58	55.61	56.75	80.11
	Flat_surface_waves	47.63	48.90	52.17	46.21	44.29	45.30	49.99	50.66	43.37
Public Datasets [1, 2, 3, 4, 5, 6, 7, 8, 9, 10, 11, 12, 13, 14, 15, 16, 17, 18, 19, 20, 21, 22, 23, 24, 25, 26, 27, 28, 29, 30, 31, 32, 33, 34, 35, 36, 37, 38, 39, 40, 41, 42, 43, 44, 45, 46, 47, 48, 49, 50, 51, 52, 53, 54, 55, 56, 57, 58, 59, 60, 61, 62, 63, 64, 65, 66, 67, 68, 69, 70, 71, 72, 73, 74, 75, 76, 77, 78, 79, 80, 81, 82, 83, 84, 85, 86, 87, 88, 89, 90, 91, 92, 93, 94, 95, 96, 97, 98, 99, 100, 101, 102, 103, 104, 105, 106, 107, 108, 109, 110, 111, 112, 113, 114, 115, 116, 117, 118, 119, 120, 121, 122, 123, 124, 125, 126, 127, 128, 129, 130, 131, 132, 133, 134, 135, 136, 137, 138, 139, 140, 141, 142, 143, 144, 145, 146, 147, 148, 149, 150, 151, 152, 153, 154, 155, 156, 157, 158, 159, 160, 161, 162, 163, 164, 165, 166, 167, 168, 169, 170, 171, 172, 173, 174, 175, 176, 177, 178, 179, 180, 181, 182, 183, 184, 185, 186, 187, 188, 189, 190, 191, 192, 193, 194, 195, 196, 197, 198, 199, 200, 201, 202, 203, 204, 205, 206, 207, 208, 209, 210, 211, 212, 213, 214, 215, 216, 217, 218, 219, 220, 221, 222, 223, 224, 225, 226, 227, 228, 229, 230, 231, 232, 233, 234, 235, 236, 237, 238, 239, 240, 241, 242, 243, 244, 245, 246, 247, 248, 249, 250, 251, 252, 253, 254, 255, 256, 257, 258, 259, 260, 261, 262, 263, 264, 265, 266, 267, 268, 269, 270, 271, 272, 273, 274, 275, 276, 277, 278, 279, 280, 281, 282, 283, 284, 285, 286, 287, 288, 289, 290, 291, 292, 293, 294, 295, 296, 297, 298, 299, 300, 301, 302, 303, 304, 305, 306, 307, 308, 309, 310, 311, 312, 313, 314, 315, 316, 317, 318, 319, 320, 321, 322, 323, 324, 325, 326, 327, 328, 329, 330, 331, 332, 333, 334, 335, 336, 337, 338, 339, 340, 341, 342, 343, 344, 345, 346, 347, 348, 349, 350, 351, 352, 353, 354, 355, 356, 357, 358, 359, 360, 361, 362, 363, 364, 365, 366, 367, 368, 369, 370, 371, 372, 373, 374, 375, 376, 377, 378, 379, 380, 381, 382, 383, 384, 385, 386, 387, 388, 389, 390, 391, 392, 393, 394, 395, 396, 397, 398, 399, 400, 401, 402, 403, 404, 405, 406, 407, 408, 409, 410, 411, 412, 413, 414, 415, 416, 417, 418, 419, 420, 421, 422, 423, 424, 425, 426, 427, 428, 429, 430, 431, 432, 433, 434, 435, 436, 437, 438, 439, 440, 441, 442, 443, 444, 445, 446, 447, 448, 449, 450, 451, 452, 453, 454, 455, 456, 457, 458, 459, 460, 461, 462, 463, 464, 465, 466, 467, 468, 469, 470, 471, 472, 473, 474, 475, 476, 477, 478, 479, 480, 481, 482, 483, 484, 485, 486, 487, 488, 489, 490, 491, 492, 493, 494, 495, 496, 497, 498, 499, 500, 501, 502, 503, 504, 505, 506, 507, 508, 509, 510, 511, 512, 513, 514, 515, 516, 517, 518, 519, 520, 521, 522, 523, 524, 525, 526, 527, 528, 529, 530, 531, 532, 533, 534, 535, 536, 537, 538, 539, 540, 541, 542, 543, 544, 545, 546, 547, 548, 549, 550, 551, 552, 553, 554, 555, 556, 557, 558, 559, 560, 561, 562, 563, 564, 565, 566, 567, 568, 569, 570, 571, 572, 573, 574, 575, 576, 577, 578, 579, 580, 581, 582, 583, 584, 585, 586, 587, 588, 589, 590, 591, 592, 593, 594, 595, 596, 597, 598, 599, 600, 601, 602, 603, 604, 605, 606, 607, 608, 609, 610, 611, 612, 613, 614, 615, 616, 617, 618, 619, 620, 621, 622, 623, 624, 625, 626, 627, 628, 629, 630, 631, 632, 633, 634, 635, 636, 637, 638, 639, 640, 641, 642, 643, 644, 645, 646, 647, 648, 649, 650, 651, 652, 653, 654, 655, 656, 657, 658, 659, 660, 661, 662, 663, 664, 665, 666, 667, 668, 669, 670, 671, 672, 673, 674, 675, 676, 677, 678, 679, 680, 681, 682, 683, 684, 685, 686, 687, 688, 689, 690, 691, 692, 693, 694, 695, 696, 697, 698, 699, 700, 701, 702, 703, 704, 705, 706, 707, 708, 709, 710, 711, 712, 713, 714, 715, 716, 717, 718, 719, 720, 721, 722, 723, 724, 725, 726, 727, 728, 729, 730, 731, 732, 733, 734, 735, 736, 737, 738, 739, 740, 741, 742, 743, 744, 745, 746, 747, 748, 749, 750, 751, 752, 753, 754, 755, 756, 757, 758, 759, 760, 761, 762, 763, 764, 765, 766, 767, 768, 769, 770, 771, 772, 773, 774, 775, 776, 777, 778, 779, 780, 781, 782, 783, 784, 785, 786, 787, 788, 789, 790, 791, 792, 793, 794, 795, 796, 797, 798, 799, 800, 801, 802, 803, 804, 805, 806, 807, 808, 809, 810, 811, 812, 813, 814, 815, 816, 817, 818, 819, 820, 821, 822, 823, 824, 825, 826, 827, 828, 829, 830, 831, 832, 833, 834, 835, 836, 837, 838, 839, 840, 841, 842, 843, 844, 845, 846, 847, 848, 849, 850, 851, 852, 853, 854, 855, 856, 857, 858, 859, 860, 861, 862, 863, 864, 865, 866, 867, 868, 869, 870, 871, 872, 873, 874, 875, 876, 877, 878, 879, 880, 881, 882, 883, 884, 885, 886, 887, 888, 889, 890, 891, 892, 893, 894, 895, 896, 897, 898, 899, 900, 901, 902, 903, 904, 905, 906, 907, 908, 909, 910, 911, 912, 913, 914, 915, 916, 917, 918, 919, 920, 921, 922, 923, 924, 925, 926, 927, 928, 929, 930, 931, 932, 933, 934, 935, 936, 937, 938, 939, 940, 941, 942, 943, 944, 945, 946, 947, 948, 949, 950, 951, 952, 953, 954, 955, 956, 957, 958, 959, 960, 961, 962, 963, 964, 965, 966, 967, 968, 969, 970, 971, 972, 973, 974, 975, 976, 977, 978, 979, 980, 981, 982, 983, 984, 985, 986, 987, 988, 989, 990, 991, 992, 993, 994, 995, 996, 997, 998, 999, 1000]	Steam	7.38	8.84	8.27	12.55	12.52	13.01	12.4	13.57	15.47
	Avalanche01	10.43	12.29	12.26	12.12	12.57	12.24	12.78	12.64	17.76
	Boil (water)	13.27	48.61	18.72	13.91	26.26	25.83	13.94	20.96	42.3
	Fountain01	19.69	26.52	18.8	23.67	20.2	20.18	21.39	27.48	22.25
	Fountain02	30.67	61.72	31.72	26.93	34.66	25.72	31.3	33.56	27.64
	Forest_fire	8.37	8.84	8.39	8.61	10.59	10.45	10.61	9.1	18.85
	Landslide01	86.08	87.72	84.94	87.06	89.67	87.82	87.24	86.31	120.2
	Landslide02	88.13	86.96	89.43	91.74	89.04	87.49	91.12	91.17	117.7
	Volcano_eruption01	5.63	5.82	5.99	5.92	6.89	5.98	5.69	5.97	5.63
	Volcano_eruption02	6.96	7.22	7.41	7.24	7.54	7.47	7.34	7.58	7.5
	Waterfall01	17.86	19.1	18.97	21.45	20.8	19.89	19.3	17.9	18.33
	Waterfall02	15.8	17.76	18	20.02	17.6	18.32	18.14	18.42	18.89
	Waterfall03	13.97	15.06	14.91	18.06	18.14	17.88	16.68	14.82	16.00
Internet	Car_smoke	8.85	10.3	10.69	10.64	10.57	10.66	10.58	9.01	10.79
	Fire_smoke	12.49	13.21	13.17	12.64	12.81	12.61	12.91	12.68	16.49
	Avalanche02	12.34	13.36	13.65	13.38	14.05	13.98	14.24	13.95	15.82
	Train	11.2	14.13	14.31	14.28	14.18	14.3	14.08	33.44	16.11
	Fireman	18.86	19.42	19.42	19.66	19.52	19.56	19.29	20.72	19.04
	Match_cube	72.53	74.65	72.93	80.50	87.40	84.32	77.22	87.88	85.09

Table 1: Low Rate Distance (Equation 9) designed for low frame rate video (Public Database and Internet). We compare our method to eight state-of-the-art algorithms using videos from our laboratory, from public datasets, and from the Internet; “Train” is a computer graphic simulation. Bold figures indicate the best performance in each row, we come first in most cases. Data shown $\times 100$ for easy reading. Note that the lower readings show higher accuracy.

used to benchmark general methods. Brox *et al.* (LDOF) [10] address large motion displacement issues using feature matching. Xu *et al.* (MDP) [11] show excellent performance on the Middlebury benchmark [9]. FlowNet [12] uses a deep neural network and achieves good results. Since the ground truth motion for natural phenomenon is unavailable we keep the original FlowNet parameters.

There is no ground truth for any of our video, so we use two measures adapted from the literature. One measure is similar to in Li *et al.* [23] who warp frame 1 using the flow, v_{12} , from frame 1 to frame 2. The warped image is compared to the second frame using mean RMS error. This measure is suitable for low video frame rates, so we call it the low rate distance (LRD):

$$\text{LRD} = \|I_2 - \text{warp}(I_1, v_{12})\|_2^2 \quad (9)$$

The second measure we used is an adapted version of the Interpolation Error (IE) suggested in [9], which is better for high frame rate video because it uses frames 1 and 3, tacitly assuming constant velocity. We compute a forward flow (frame 1 to 3) and a backward flow (frame 3 to 1), then warp frames 1 and 3, taking the average wherever the flow is consistent, and the forward flow elsewhere. Again, we use RMS error but now call it high rate distance (HRD):

$$\text{HRD} = \|I_2 - \text{merge}[\text{warp}(I_1, v_{13}), \text{warp}(I_3, v_{31})]\|_2^2 \quad (10)$$

Results for all videos are shown in Table 1 for LRD, and Table 2 for HRD. The tables show that our approach consistently outperforms other methods: we come first in most cases. In fact, due to space limitations, we removed many cases in which we were first; full tables can be found in the supplementary material. These larger tables show that, on average, our method outperforms all others by at least 17% when using LRD and 31% when using HRD.

Figure 3 shows qualitative results which uses a colour wheel to visualise flow. The waterfall provides a useful example. Our result shows a predominantly downward fall (orange colour), but captures flow into and away from the fall (cyan) at the top and bottom; these are the cyan regions. All

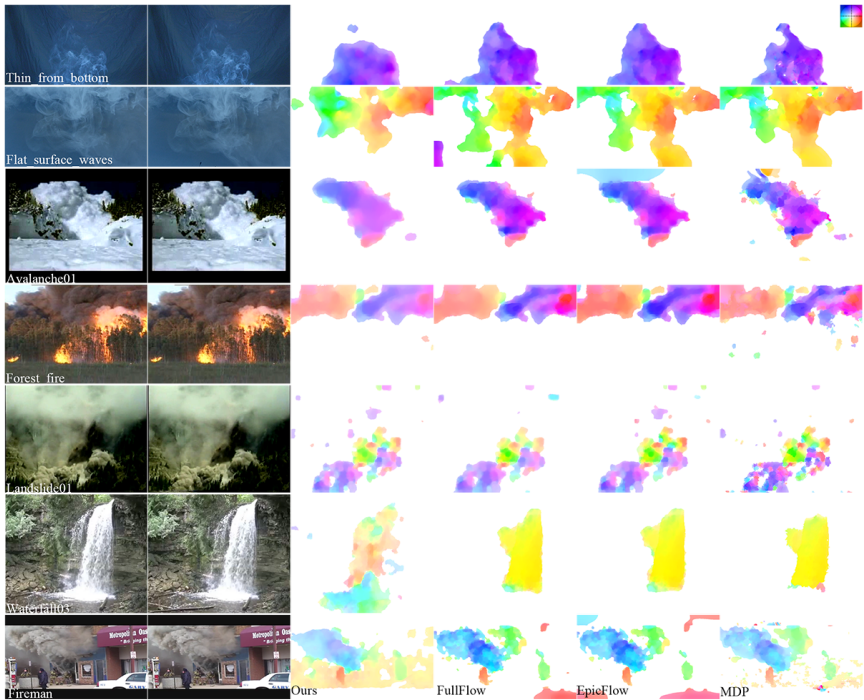


Figure 3: Qualitative results for selected phenomena: Left two columns show input frames, subsequent columns show dense flow visualizations for selected contemporary alternatives. From left to right: Ours, FullFlow [30], EpicFlow [29], MDP [40]. We use colour to indicate direction and magnitude of the flow, see top right for key.



Figure 4: Qualitative comparison of segmentations. Left to right: original image; hand drawn ground truth (green); our approach (blue); Teney *et al.* [35] (cyan); Papazoglou *et al.* (FS) [27] (magenta); and SegFlow [10] (yellow). Our segmentation yields better representative for the natural phenomena given either clean or complex background. Segflow is able to segment some but not all cases, so some images have no segmentations shown.

	Ours	Teney [15]	FS [14]	SegFlow [10]
Car_smoke	77.78	76.76	68.10	69.11
Fire_smoke	89.75	85.46	59.91	51.27
Train	94.21	86.41	50.01	56.06
Avalanche02	79.49	68.10	57.76	50.20
Waterfall03	89.10	86.35	80.72	68.73
Forest_fire	82.44	67.10	66.27	57.39
Fireman	92.35	89.98	56.64	87.01
Match_cube	95.40	81.90	87.89	58.38

Table 3: Average Rand Index (%) evaluation on segmentations for our method and three other state-of-the-art unsupervised algorithms.

map of topographical features to capture the ‘gist’ of shape, and therefore the ‘gist’ of global flow. We explain our flow results by posulating that our global, sparse flow we obtain provides a strong prior constraint for dense, local flow, in the sense of “picking” a useful starting point for search. We explain our segmentation results by appeal to the diffuse nature of the phenomena we deal with – particles move freely so that features are highly blurred and transient – our skeleton is robust to such movements because they change overall shape only a little.

Like any method, ours has its limitations, each of which provide interesting avenues for future work. Our motion estimator is designed for natural phenomena rather than, say, articulated objects, so more general applicability is an open question. A perhaps subtle problem is that we tacitly assume the spatial distance between skeletal limbs in a single frame exceeds the distance moved by a single skeletal limb between frames. We have yet to conduct a detailed analysis of this, but preliminary studies suggest to us there is Nyquist-like problem here that might be solved using a coarse-to-fine approach over different scales of skeleton. Although we achieve excellent segmentation results, above state-of-the-art alternatives, it is clear more work needs to be done. We favour an iterative scheme in which segmentation and motion are jointly estimated. Finally, we have only just begun to explore the possibilities of using a skeleton for Computer Graphics. Motion editing being the motivation application is a particular application that would benefit from having a skeleton at hand provides a mid-level model that could be built into an interactive tool in which users drag skeletons, or even draw them – but such work is for another paper.

Our general conclusions from this work are: (i) brightness constancy can and should be replaced by more appropriate assumptions when needed; (ii) assumptions regarding physical behaviour do not have to be strong assumptions; and (iii) global behaviour is useful for constraining local behaviour.

7 Acknowledgements

This research is partly funded by CAMERA, the RCUK Centre for the Analysis of Motion, Entertainment Research and Applications, EP/M023281/1.

References

- [1] Radhakrishna Achanta, Appu Shaji, Kevin Smith, Aurelien Lucchi, Pascal Fua, and Sabine Süsstrunk. Slic superpixels compared to state-of-the-art superpixel methods. *IEEE transactions on pattern analysis and machine intelligence*, 34(11):2274–2282, 2012.
- [2] Lakshman Anumolu and Imaduddin Ahmed. Simulation of smoke in openfoam framework. 2012.
- [3] Didier Auroux and Jérôme Fehrenbach. Identification of velocity fields for geophysical fluids from a sequence of images. *Experiments in Fluids*, 50(2):313–328, 2011.
- [4] Simon Baker, Daniel Scharstein, JP Lewis, Stefan Roth, Michael J Black, and Richard Szeliski. A database and evaluation methodology for optical flow. *International Journal of Computer Vision*, 92(1):1–31, 2011.
- [5] Frédéric Barbaresco and Bernard Monnier. Rain clouds tracking with radar image processing based on morphological skeleton matching. In *Image Processing, 2001. Proceedings. 2001 International Conference on*, volume 1, pages 830–833. IEEE, 2001.

- [6] Michael J Black and Paul Anandan. The robust estimation of multiple motions: Parametric and piecewise-smooth flow fields. *Computer vision and image understanding*, 63(1):75–104, 1996.
- [7] Thomas Brox and Jitendra Malik. Large displacement optical flow: descriptor matching in variational motion estimation. *Pattern Analysis and Machine Intelligence, IEEE Transactions on*, 33(3):500–513, 2011.
- [8] Thomas Brox, Andrés Bruhn, Nils Papenberg, and Joachim Weickert. High accuracy optical flow estimation based on a theory for warping. In *Computer Vision-ECCV 2004*, pages 25–36. Springer, 2004.
- [9] Qifeng Chen and Vladlen Koltun. Full flow: Optical flow estimation by global optimization over regular grids. *arXiv preprint arXiv:1604.03513*, 2016.
- [10] J. Cheng, Y.-H. Tsai, S. Wang, and M.-H. Yang. Segflow: Joint learning for video object segmentation and optical flow. In *IEEE International Conference on Computer Vision (ICCV)*, 2017.
- [11] Thomas Corpetti, Etienne Mémin, and Patrick Pérez. Estimating fluid optical flow. In *Pattern Recognition, 2000. Proceedings. 15th International Conference on*, volume 3, pages 1033–1036. IEEE, 2000.
- [12] Konstantinos G Derpanis, Matthieu Lecce, Kostas Daniilidis, and Richard P Wildes. Dynamic scene understanding: The role of orientation features in space and time in scene classification. In *Computer Vision and Pattern Recognition (CVPR), 2012 IEEE Conference on*, pages 1306–1313. IEEE, 2012.
- [13] Ashish Doshi and Adrian G Bors. Robust processing of optical flow of fluids. *Image Processing, IEEE Transactions on*, 19(9):2332–2344, 2010.
- [14] Alexey Dosovitskiy, Philipp Fischer, Eddy Ilg, Philip Hausser, Caner Hazirbas, Vladimir Golkov, Patrick van der Smagt, Daniel Cremers, and Thomas Brox. FlowNet: Learning optical flow with convolutional networks. In *Proceedings of the IEEE International Conference on Computer Vision*, pages 2758–2766, 2015.
- [15] Ravi Garg, Anastasios Roussos, and Lourdes Agapito. A variational approach to video registration with subspace constraints. volume 104, pages 286–314. Springer, 2013.
- [16] Bernard Ghanem and Narendra Ahuja. Extracting a fluid dynamic texture and the background from video. In *Computer Vision and Pattern Recognition, 2008. CVPR 2008. IEEE Conference on*, pages 1–8. IEEE, 2008.
- [17] Bernard Ghanem and Narendra Ahuja. Maximum margin distance learning for dynamic texture recognition. In *European Conference on Computer Vision*, pages 223–236. Springer, 2010.
- [18] James Gregson, Ivo Ihrke, Nils Thuerey, Wolfgang Heidrich, et al. From capture to simulation-connecting forward and inverse problems in fluids. *ACM Transactions on Graphics*, 33, 2014.
- [19] Berthold K Horn and Brian G Schunck. Determining optical flow. In *1981 Technical Symposium East*, pages 319–331. International Society for Optics and Photonics, 1981.
- [20] Yu Ji, Jinwei Ye, and Jingyi Yu. Reconstructing gas flows using light-path approximation. In *Computer Vision and Pattern Recognition (CVPR), 2013 IEEE Conference on*, pages 2507–2514. IEEE, 2013.
- [21] V Lakshmanan, R Rabin, and V DeBrunner. Multiscale storm identification and forecast. *Atmospheric research*, 67:367–380, 2003.
- [22] Chuan Li, David Pickup, Thomas Saunders, Darren Cosker, David Marshall, Peter Hall, and Philip Willis. Water surface modeling from a single viewpoint video. *Visualization and Computer Graphics, IEEE Transactions on*, 19(7):1242–1251, 2013.
- [23] Feng Li, Liwei Xu, Philippe Guyenne, and Jingyi Yu. Recovering fluid-type motions using navier-stokes potential flow. In *Computer Vision and Pattern Recognition (CVPR), 2010 IEEE Conference on*, pages 2448–2455. IEEE, 2010.
- [24] Peter Ochs, Jitendra Malik, and Thomas Brox. Segmentation of moving objects by long term video analysis. *IEEE transactions on pattern analysis and machine intelligence*, 36(6):1187–1200, 2014.
- [25] Abhijit S Ogale, Cornelia Fermuller, and Yiannis Aloimonos. Motion segmentation using occlusions. *IEEE Transactions on Pattern Analysis and Machine Intelligence*, 27(6):988–992, 2005.
- [26] Makoto Okabe, Ken Anjyo, and Rikio Onai. Extracting fluid from a video for efficient post-production. In *Proceedings of the Digital Production Symposium*, pages 53–58. ACM, 2012.
- [27] Anestis Papazoglou and Vittorio Ferrari. Fast object segmentation in unconstrained video. In *Proceedings of the IEEE International Conference on Computer Vision*, pages 1777–1784, 2013.
- [28] W.M. Rand. Objective criteria for the evaluation of clustering methods. *Journal of the American Statistical Association*, 66(336):846–850, 1971.
- [29] Jerome Revaud, Philippe Weinzaepfel, Zaid Harchaoui, and Cordelia Schmid. Epicflow: Edge-preserving

- interpolation of correspondences for optical flow. In *Proceedings of the IEEE Conference on Computer Vision and Pattern Recognition*, pages 1164–1172, 2015.
- [30] Hidetomo Sakaino. Fluid motion estimation method based on physical properties of waves. In *Computer Vision and Pattern Recognition, 2008. CVPR 2008. IEEE Conference on*, pages 1–8. IEEE, 2008.
 - [31] Laura Sevilla-Lara, Deqing Sun, Varun Jampani, and Michael J Black. Optical flow with semantic segmentation and localized layers. In *IEEE Conference on Computer Vision and Pattern Recognition (CVPR)*, 2016.
 - [32] Nitesh Shroff, Pavan Turaga, and Rama Chellappa. Moving vistas: Exploiting motion for describing scenes. In *Computer Vision and Pattern Recognition (CVPR), 2010 IEEE Conference on*, pages 1911–1918. IEEE, 2010.
 - [33] Deqing Sun, Stefan Roth, and Michael J Black. Secrets of optical flow estimation and their principles. In *Computer Vision and Pattern Recognition (CVPR), 2010 IEEE Conference on*, pages 2432–2439. IEEE, 2010.
 - [34] Damien Teney and Matthew Brown. Segmentation of dynamic scenes with distributions of spatiotemporally oriented energies. In *25th British Machine Vision Conference, BMVC 2014*, 2014.
 - [35] Damien Teney, Matthew Brown, Dmitry Kit, and Peter Hall. Learning similarity metrics for dynamic scene segmentation. In *Proceedings of the IEEE Conference on Computer Vision and Pattern Recognition*, pages 2084–2093, 2015.
 - [36] Carlo Tomasi and Roberto Manduchi. Bilateral filtering for gray and color images. In *Computer Vision, 1998. Sixth International Conference on*, pages 839–846. IEEE, 1998.
 - [37] Daniel Alejandro Vila, Luiz Augusto Toledo Machado, Henri Laurent, and Ines Velasco. Forecast and tracking the evolution of cloud clusters (fortracc) using satellite infrared imagery: Methodology and validation. *Weather and Forecasting*, 23(2):233–245, 2008.
 - [38] Guojie Wang, Damien Garcia, Yi Liu, Richard De Jeu, and A Johannes Dolman. A three-dimensional gap filling method for large geophysical datasets: Application to global satellite soil moisture observations. *Environmental Modelling & Software*, 30:139–142, 2012.
 - [39] Philippe Weinzaepfel, Jerome Revaud, Zaid Harchaoui, and Cordelia Schmid. DeepFlow: Large displacement optical flow with deep matching. In *IEEE International Conference on Computer Vision (ICCV)*, Sydney, Australia, December 2013. URL <http://hal.inria.fr/hal-00873592>.
 - [40] Chenliang Xu, Caiming Xiong, and Jason J Corso. Streaming hierarchical video segmentation. In *European Conference on Computer Vision*, pages 626–639. Springer, 2012.
 - [41] Li Xu, Jiaya Jia, and Yasuyuki Matsushita. Motion detail preserving optical flow estimation. *Pattern Analysis and Machine Intelligence, IEEE Transactions on*, 34(9):1744–1757, 2012.
 - [42] Tianfan Xue, Michael Rubinstein, Neal Wadhwa, Anat Levin, Fredo Durand, and William T Freeman. Refraction wiggles for measuring fluid depth and velocity from video. In *Computer Vision–ECCV 2014*, pages 767–782. Springer, 2014.